JOURNAL OF GEOPHYSICAL RESEARCH, VOL. 112, C12013, doi:10.1029/2006JC003978, 2007

Ice, Cloud, and land Elevation Satellite (ICESat) over Arctic sea ice: Retrieval of freeboard

R. Kwok,[1] G. F. Cunningham,[1] H. J. Zwally,[2] and D. Yi[3]

Received 17 October 2006; revised 19 March 2007; accepted 25 April 2007; published 21 December 2007.

[1] Total freeboard (snow and ice) of the Arctic Ocean sea ice cover is derived using Ice, Cloud, and land Elevation Satellite (ICESat) data from two 35-day periods: one during the fall (October–November) of 2005 and the other during the winter (February–March) of 2006. Three approaches are used to identify near-sea-surface tiepoints. Thin ice or open water samples in new openings, typically within 1–2 cm of the sea surface, are used to assess the sea surface estimates. Results suggest that our retrieval procedures could provide consistent freeboard estimates along 25-km segments with uncertainties of better than 7 cm. Basin-scale composites of sea ice freeboard show a clear delineation of the seasonal ice zone in the fall. Overall, the mean freeboards of multiyear (MY) and first-year (FY) ice are 35 cm and 14 cm in the fall, and 43 cm and 27 cm in the winter. The increases of ~9 cm and ~12 cm on MY and FY sea ice are associated with the 4 months of ice growth and snow accumulation between data acquisitions. Since changes in snow depth account for >90% of the seasonal increase in freeboard on MY ice, it dominates the seasonal signal. Our freeboard estimates are within 10 cm of those derived from available snow/ice thickness measurements from ice mass balance buoys. Examination of the two residual elevations fields, after the removal of the sea ice freeboard contribution, shows coherent spatial patterns with a standard deviation (S.D.) of ~23 cm. Differencing them reduces the variance and gives a near random field with a mean of ~2 cm and a standard deviation of ~14 cm. While the residual fields seem to be dominated by the static component of unexplained sea surface height and mean dynamic topography (S.D. ~23 cm), the difference field reveals the magnitude of the time-varying components as well as noise in the ICESat elevations (S.D. ~10 cm).

Citation: Kwok, R., G. F. Cunningham, H. J. Zwally, and D. Yi (2007), Ice, Cloud, and land Elevation Satellite (ICESat) over Arctic sea ice: Retrieval of freeboard, *J. Geophys. Res.*, *112*, C12013, doi:10.1029/2006JC003978.

1. Introduction

[2] At this writing, Ice, Cloud, and land Elevation Satellite (ICESat) has successfully completed ten data acquisition campaigns since its January launch of 2003. Each operational campaign consists of a laser-on period that spans approximately one 33-day subcycle of the 91-day repeat orbit. The interval between campaigns is ~3 months. This sampling strategy is employed to allow for detection of seasonal and interannual changes of the global ice cover. Overviews of the ICESat mission are given by *Zwally et al.* [2002] and *Schutz et al.* [2005]. A compilation of the recent scientific results can be found in a special section on ICESat in the *Geophysical Research Letters*.

[1]Jet Propulsion Laboratory, California Institute of Technology, Pasadena, California, USA.
[2]Cryospheric Sciences Branch, NASA Goddard Space Flight Center, Greenbelt, Maryland, USA.
[3]SGT, Inc., NASA Goddard Space Flight Center, Greenbelt, Maryland, USA.

0148-0227/07/2006JC003978$09.00

[3] The subject of this paper pertains to the use of ICESat data for Arctic Ocean studies. Previous examinations of the ICESat data set of Arctic sea ice given by *Kwok et al.* [2004, 2006] have provided general overviews. Of particular geophysical interest is the potential of obtaining estimates of sea ice freeboard and thickness from the altimetric profiles. Because of the importance of thickness in sea ice mass balance and in the surface heat and energy budget, remote determination of ice thickness at almost any spatial scale has long been desired. Current spaceborne sensors, however, can see only radiation emitted or scattered from the top surface or the volume within the top few tens of centimeters of the ice and do not see the lower surface; this is an obstacle to the direct observations of ice thickness. An alternative approach has been to use altimetric freeboard along with the assumption of hydrostatic equilibrium to determine ice thickness. The first geophysical results of ice freeboard/thickness estimates from spaceborne radar altimeters are given by *Laxon et al.* [2003]. Specular radar returns from open water/thin ice provide the necessary sea surface references: this forms the algorithm basis for derivation of freeboard estimates for the planned CryoSat-2 mission. For ICESat, one approach of freeboard retrieval in

the published literature is discussed by *Kwok et al.* [2004] and another by *Forsberg and Skourup* [2005]; these are presented as part of an initial assessment of ICESat data. Many investigators are working toward accurate freeboard and thickness retrievals for addressing current gaps and for providing future estimates of these key climate parameters.

[4] The focus of this paper is on the retrieval of freeboard from two Arctic Ocean ICESat data sets, one acquired during the fall of 2005 and the other during the winter of 2006. The objectives are to provide a detailed description of the geophysical issues and to determine what is achievable in terms of the estimation of this parameter. The topic of conversion to sea ice thickness is not addressed. A crucial first step is to identify local tiepoints of the sea surface in the altimeter data because of the large uncertainties our knowledge of sea surface height compared to that required for accurate determination of freeboard. We offer three approaches for acquiring such tiepoints. The geophysical basis for identifying such points and the uncertainties associated with their acquisitions are addressed. The first approach uses young ice in new openings identified in ICESat profiles and SAR imagery while the other two are derived solely from ICESat data. Their relative merits are discussed and the resulting fields of freeboard estimates are assessed.

[5] This paper is organized as follows. Section 2 describes the ICESat products and ancillary data sets used in our analyses. The relationships between ICESat elevation, freeboard, sea surface height and tiepoints are described in section 3. The next section discusses the data filters used in removing the unreliable and contaminated ICESat data samples. The three approaches for acquiring sea surface tiepoints and their uncertainties are discussed in section 5. In section 6, basin-scale maps of the freeboard and their distributions are constructed using the available sea level tiepoints. The consistencies of these two freeboard composites are examined in terms of their spatial variability and changes during the three months between acquisitions. The retrieved freeboards are compared with those derived from available snow and ice thicknesses reported by ice mass balance buoys. Section 7 discusses the variance associated with the unexplained static and time-varying components of the sea surface that are obtained after the sea ice freeboard is removed. The last section summarizes the paper.

2. Data Description

2.1. ICESat Data

[6] The two ICESat sea ice data sets used in this paper are acquired by Laser 3d and Laser 3e. These laser campaigns span a period of 35 days during the fall of 2005 (21 October through 24 November) and 34 days during the winter of 2006 (22 February through 27 March). The ICESat data products are of release 428, the latest and best release available in terms of orbit and attitude determination at the time of this writing. Henceforth these two laser operational periods will be referred to as ON05 and FM06.

2.2. Other Data Sets

[7] The RADARSAT imagery used here are calibrated, processed, and archived at the Alaska Satellite Facility (ASF) in Fairbanks. The RADARSAT C-band synthetic aperture radar (SAR) transmits and receives horizontally polarized radiation (HH). The image data used here (resolution $\sim$ 150 m) are acquired by the instrument operating in one of the ScanSAR modes that illuminates a ground swath of 460 km. The RADARSAT images of the Arctic Ocean are acquired as part of a NASA program to study the small-scale kinematics of sea ice. Since November 1996, there is near 3-day coverage of the western Arctic within the ASF reception mask. To support ICESat studies, this coverage frequency has been increased. During the two periods of interest here, there is almost daily coverage in the high Arctic. Gridded fields of multiyear ice fractions are from the analysis of QuikSCAT data [*Kwok*, 2004]. QuikSCAT is a moderate resolution wide-swath (1800 km) K_u-band scatterometer that provides daily coverage of the Arctic Ocean at V and H polarizations at incidence angles of 53° and 45°. Ice motion shown here is derived from satellite passive microwave observations [*Kwok et al.*, 1998]. The 6-hourly sea level pressure (SLP) fields are from the National Centers for Environmental Prediction (NCEP)-National Center for Atmospheric Research (NCAR) analysis products.

3. ICESat Elevations, Freeboard, Sea Surface, and Tiepoints

[8] As alluded to earlier, tiepoints along the ICESat profiles are necessary for providing local references to the sea surface due to our lack of sufficiently accurate knowledge of the time-varying sea surface height. This section describes: (1) the geometric relationships between ICESat elevation, freeboard, and sea surface height; (2) how an initial estimate of sea surface height is constructed; and (3) how local sea surface references are used to estimate the mean freeboard over 25-km segments of ICESat data. The procedures for identifying these sea surface tiepoints are provided in section 5.

[9] We define the freeboard to be the vertical distance between the air-snow interface and the local sea surface. For the Arctic Ocean, the total freeboard consists generally of a snow layer superimposed on the freeboard of floating sea ice. This total freeboard height, h_f, above the sea surface can be written as the sum of two terms (Figure 1a),

$$h_f = h_{fs} + h_{fi} \tag{1}$$

where h_{fs} and h_{fi} are the thicknesses of the snow and ice layers above the sea surface. Throughout this paper, freeboard generally refers to the total freeboard, h_f, unless noted otherwise.

[10] The total freeboard, h_f, is the difference between surface elevation, h_s, as measured by an altimeter and the sea surface height, h_{ssh},

$$h_f(x, t_i) = h_s(x, t_i) - h_{ssh}(x, t_i). \tag{2}$$

Typically, both h_s and h_{ssh} are measured relative to the level a particular reference ellipsoid. In the case of ICESat, the TOPEX/Poseidon ellipsoid is used. Further, the time-varying sea surface height can be decomposed into

$$h_{ssh}(x, t) = h_g(x, t) + h_a(x, t) + h_T(x, t) + h_d(x, t) + O^2. \tag{3}$$

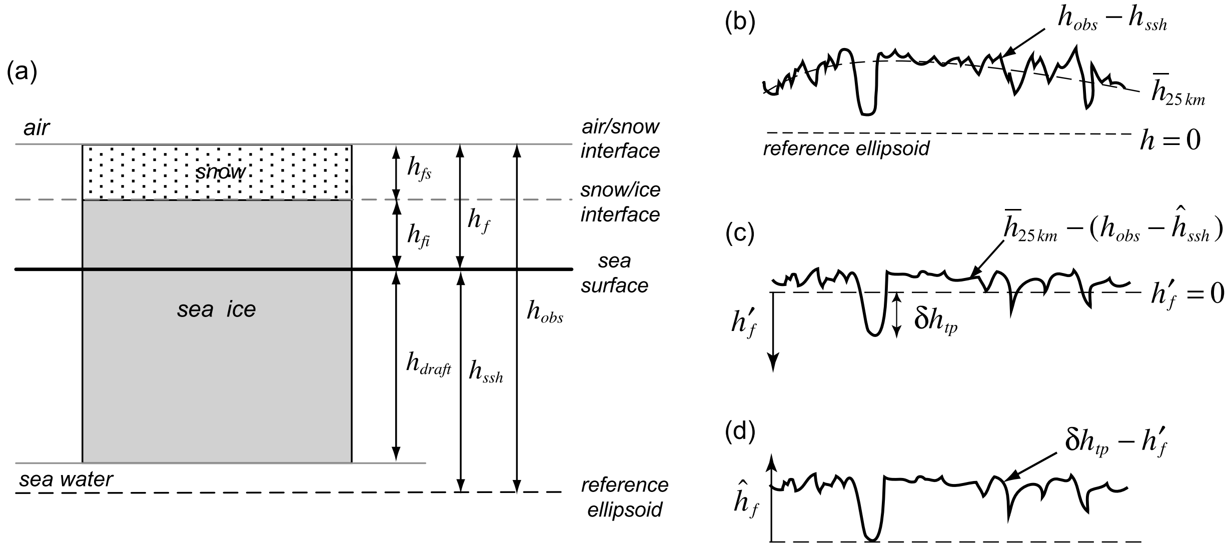

Figure 1. Schematics showing the variables discussed in section 3.

In this equation, h_g is associated with geoid undulations, h_a represents the sea surface response to atmospheric pressure loading, h_T is from tidal contributions, h_d is the dynamic topography associated with geostrophic surface currents, and higher-order terms. All terms vary in time and space and possess their own characteristic length scales. The reader is referred to *Kwok et al.* [2006] for a brief discussion of the sea surface models and the expected uncertainties of each of these terms.

[11] Defining the estimation error of sea surface height, $\tilde{h}_{ssh}$, as

$$\tilde{h}_{ssh} = \hat{h}_{ssh} - h_{ssh}, \tag{4}$$

where $\hat{h}_{ssh}$ and h_{ssh} are the estimated and true sea surface elevations, *Kwok et al.* [2006] show that the residuals in h_{ssh} (after the removal of modeled h_g, h_a, and h_T) are much greater than the expected magnitude of h_f in equation (2), i.e., $E[\tilde{h}^2_{ssh}] > E[h^2_f]$. For one ICESat campaign in February/March 2004, they show that even after the removal of the best static geoid, modeled tides, and effects due to atmospheric loading (i.e., $\hat{h}_{ssh}$), the resulting standard deviation of $\tilde{h}_{ssh}$ is ~38 cm; this can be compared to the smaller variability of the total freeboard, h_f, at ~25 cm. Thus, even though estimates of all these contributions are available, it suffices to say that our current knowledge of these terms is inadequate for accurate computation of freeboard.

[12] In the following analyses we first remove the 25-km running mean of $h_{obs} - \hat{h}_{ssh}$ (written as $\bar{h}_{25km}$; see Figure 1b) to obtain an improved estimate of the unbiased (zero mean) elevation of the freeboard, h'_f (depicted in Figure 1c),

$$h'_f = \bar{h}_{25km} - \left(h_{obs} - \hat{h}_{ssh}\right), \tag{5}$$

where h_{obs} are the elevation estimates from ICESat. This is written such that the elevations below $\bar{h}_{25km}$ are positive. The assumption is that this 25-km running mean $\bar{h}_{25km}$, a smoothed version of h_{obs}-$\hat{h}_{ssh}$ (Figure 1b), captures the spatial variability (albeit a biased estimate) of the residuals of h_{ssh} (i.e., $\tilde{h}_{ssh} \approx \bar{h}_{25km}$); and, that the difference in equation (5) (i.e., h'_f) is a better starting point for estimating the local sea surface references for freeboard estimation (Figure 1c). Implicit in this step is the assumption that the higher-frequency variability of $\tilde{h}_{ssh}$ is small; the validity of this assumption is revisited in section 7. At a spacing of ~170 m between laser shots, each 25-km ICESat segment contains ~150 individual elevation samples and gives a relative good estimate of the mean. In equation (5), the larger-amplitude, longer-wavelength variability due to $\tilde{h}_{ssh}$ is removed and the remaining elevation variability is due mostly to sea ice freeboard.

[13] With h'_f, the local freeboard estimates, $\hat{h}_f$, along 25-km segments of ICESat profiles, are then calculated by an adjustment to h'_f (Figure 1d),

$$\hat{h}_f = \delta h_{tp} - h'_f. \tag{6}$$

Here δh_{tp}(subscript *tp* for tiepoint), the local sea surface reference, is measured relative to the profile defined by $\bar{h}_{25km}$. The three approaches used to identify the sea surface tiepoints (references) in ICESat elevation and reflectivity profiles are discussed in section 5. In addition, these sea surface tiepoints also provide an improved estimate of the local sea surface elevation, h_{ssh}' that can be calculated as follows:

$$h'_{ssh} = \bar{h}_{25km} - \delta h_{tp} + \hat{h}_{ssh}. \tag{7}$$

The definitions and notations described in this section will be used throughout this paper.

[14] It is also important to note that in the following, we assume the ICESat elevations, h_{obs}, to represent the average elevation over the ICESat laser footprint of ~70 m. In the range determination process, the peak location of a Gaussian fitted to the GLAS echo waveform is used to determine the centroid of the surface return and thus its range. This computed range is used to estimate the elevation. Since this process tracks the waveform, the estimate should be a close

representation of the mean surface elevation within the footprint assuming a Lambertian surface, i.e., a diffuse surface for which the reflectance is constant for any angle of reflection. Since snow covered surfaces can be assumed to be Lambertian, this is a reasonable assumption. If specular or quasispecular surfaces such as very smooth water surfaces are present, the estimated height would be biased by the elevation of these surfaces. Unambiguous specular returns (very small percentage of the data) are removed in our filtering process below. The case for a mixture of surfaces, ice with different reflectance, is discussed in section 5.

4. Data Filtering

[15] For filtering unreliable elevation estimates, we use three instrument and waveform-derived parameters in the ICESat data products: *i_reflctUcorr* (R), *i_gainSet1064* (G), and *i_SeaIceVar* (S). Detailed descriptions of these parameters are given by *Brenner et al.* [2003]. Briefly, R is the surface reflectivity and is the ratio of the received energy, after it has been scaled for range, and transmitted energy; the reflectivity is not a calibrated quantity because of uncompensated atmospheric effects and attenuation. G is the time-varying gain setting of the GLAS detector; and S is the difference between the fitted Gaussian and that of the received waveform. These parameters provide qualitative measures of the reliability of the retrieved elevation. A high G indicates that the signal-to-noise ratio (SNR) is low and thus the likelihood of reduced surface return because of scattering by atmospheric constituents (clouds, water vapor, etc.). The detector gain for the instrument varies between 7 and 250. All samples with $G > 30$ are removed. This filter is intended to remove unreliable samples with low SNR that are contaminated by atmospheric scattering. S is a measure of the deviation of the received waveform from an expected Gaussian-like return; the uncertainty of the elevation of any waveform that is non-Gaussian is probably higher. Higher S indicates a larger deviation and all samples with $S > 60$ are not used. For both G and S, the thresholds are selected such that all retrieved elevations with G or S greater than 1σ above the mean of their sample distribution over the Arctic Ocean are removed.

[16] A fraction of the waveforms are saturated because of the limited dynamic range of the instrument. Saturation can be caused by: (1) the natural reflectivity of the surface and (2) the time-varying transmitted laser pulse energy associated with the age and particular characteristic of each GLAS laser. The current product release includes corrections for moderately saturated surface returns. For quasispecular returns from very smooth ice or open water, where $R > 1$, the waveforms distortions are typically severe and the retrieved elevations are unreliable. Thus we filter out all ICESat samples with $R > 1$. Analyzed ice concentration products from AMSR are used to remove areas with less than 30% sea ice coverage and a high-resolution (1 km) land mask is used to remove non-sea-ice samples.

5. Estimation of Local Sea Surface Height

[17] In this section, we discuss three approaches to identify and select ICESat samples for use as sea surface references. At the location of these tiepoints, using the notation in section 3: $h_f' = \delta h_{tp}$ and $\hat{h}_f = 0$; and $|\delta h_{tp}|$ is the level of both the freeboard and sea surface relative to $\bar{h}_{25km}$; that is, the terms freeboard and sea surface refer to the same vertical distance as depicted in Figure 1c.

5.1. New Openings ($\delta h_{tp} = H_{op}$)

[18] This approach is first described by *Kwok et al.* [2004, 2006]. It identifies samples of new ice that are less than several days old for use as local sea level reference (Figure 2). The first step in the procedure involves locating potential openings by visual inspection of the ICESat elevation profiles h_f'. Openings appear as segments with well-defined local elevation minima, usually less than several kilometers in length, flanked by step edges. The heights of these steps depend on the freeboard of the adjacent ice. Once these segments are identified, the age of these samples is determined by establishing the approximate time of the opening event using near-coincident RADARSAT imagery. When the widths of the openings are within the resolving capability of the radar, new openings or fractures in the ice cover typically appear as areas of low backscatter that are easily recognizable in a sequence of RADARSAT imagery. Two examples in Figure 2 show the radar images acquired before and after the ice cover opens. Figure 2 also shows two 80-km ICESat elevation/reflectivity profiles that are within several hours of the closest RADARSAT acquisitions. In these examples, the time separation between the images of 21.5 hours (0.9 days) and 31.95 hours (1.3 days) tell us that the age of the ice in both leads are on average less than a day old. As discussed below, these openings should have a thickness of $<\sim$10 cm or freeboard of 1$-$2 cm.

[19] In the absence of denser temporal coverage, uncertainty in the age of the openings is half the sampling interval. We select as tiepoints only those openings that are less than 1 day old using RADARSAT images with 2-day sampling interval. With 2-day imaging of the ice cover, the average uncertainty in ice age is 1 day. The corresponding uncertainty in sea level determined using these samples as sea level tiepoints is small. Under winter Arctic conditions, initial ice growth in leads is fast but slows as the ice thickens. For instance, using Lebedev's parameterization of sea ice growth and assuming an ambient air temperature of $-30°$C, the ice thickness of 2-day-old openings is $\sim$15 cm with a corresponding ice freeboard of less than 2 cm. That is, the new ice in these openings are within 2 cm of the sea surface. Errors in the determination of the sea surface associated with uncertainties in the thickness estimates are small since only $\sim$11% of the floating ice is above the ocean surface. Since the mean age of the distribution of openings is only one day instead of two, the estimate of 2 cm provides a upper limit on the error in the sea surface estimate. Also, this level of uncertainty can be compared to the precision in the ICESat elevation of $\sim$2 cm.

[20] Along the profiles, the low-reflectivity and low-elevation points are selected visually; local elevation spikes within an open lead are not included. Thin ice samples identified using this approach are unambiguous and can be regarded as the highest-quality tiepoints for freeboard retrieval. However, this procedure is tedious for processing

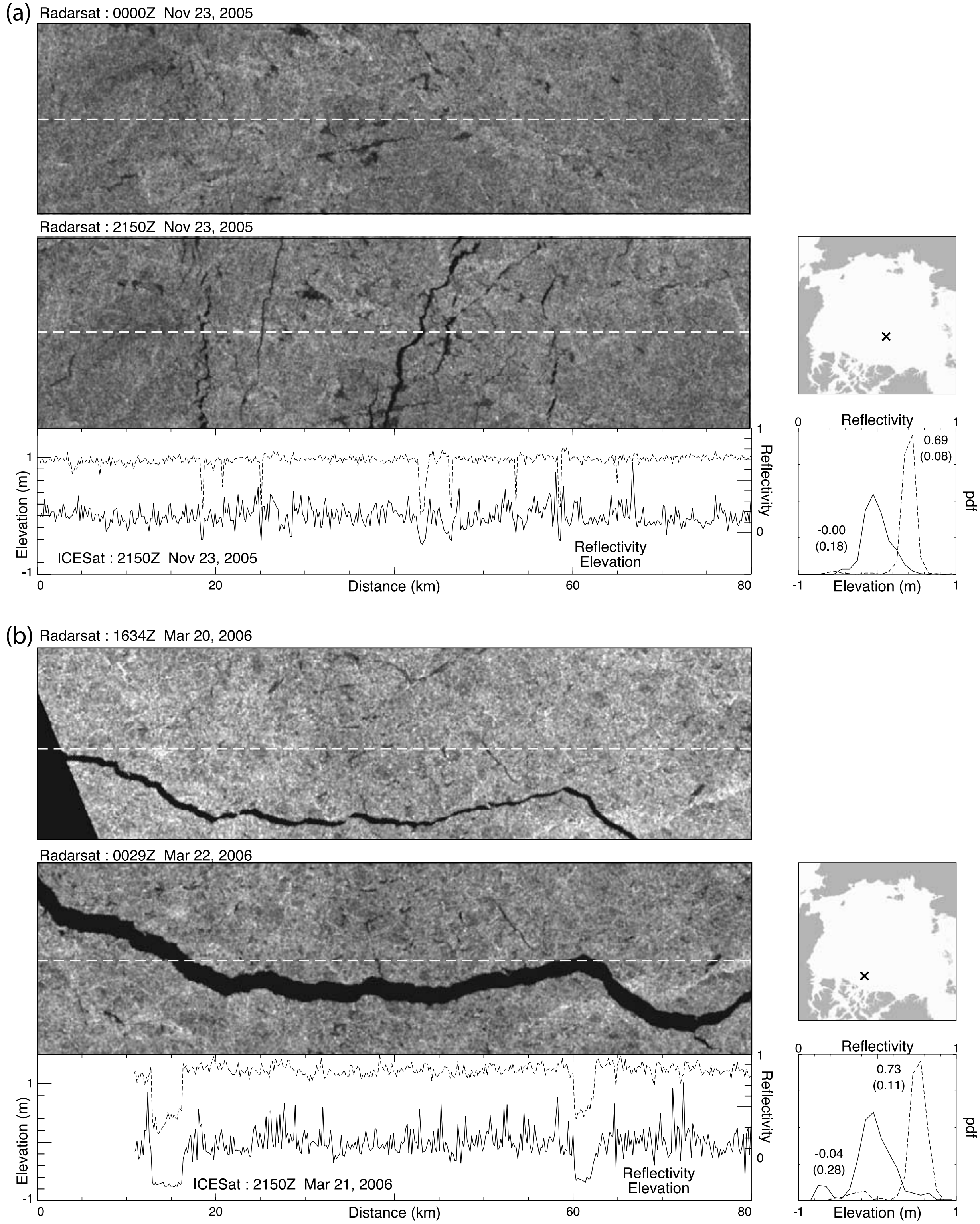

Figure 2. Two examples of new openings identified in near-coincident RADARSAT and ICESat acquisitions: (a) 23 November 2005 and (b) 22 March 2006. Openings in the ice cover can be seen as new areas of low backscatter observed in RADARSAT imagery. The ICESat track is shown as a dashed line; direction of flight is from left to right. The time separation between the ICESat and RADARSAT overflights can be computed from the date/time on the plots. A cross marks the approximate geographic location of the 80-km profile of ICESat elevations (solid line) and reflectivity (dashed line) on the Arctic map. A 25-km running mean has been removed from each elevation sample. Distributions of elevation and reflectivity of the samples are shown in the right-hand plot. (RADARSAT imagery ©CSA 2004.)

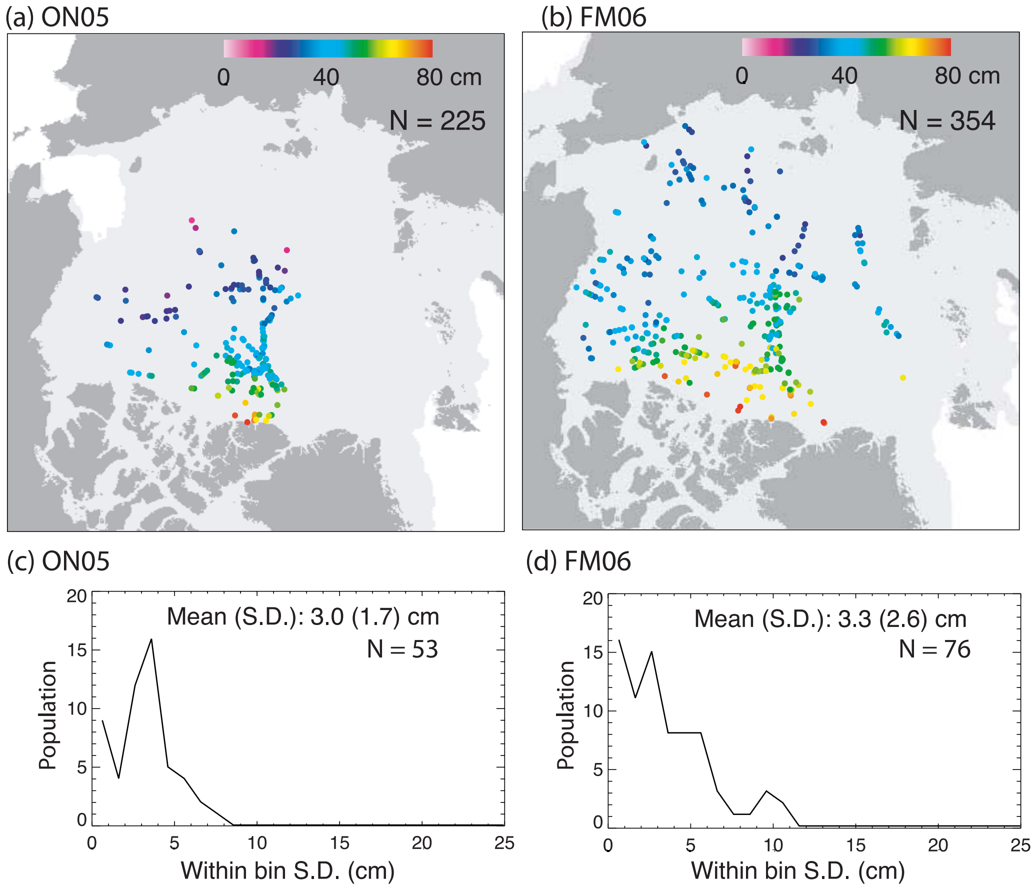

Figure 3. Sea ice freeboard adjacent to openings (<2 days old) identified in ICESat/RADARSAT data. (a) ON05. (b) FM06. (c) Histogram of standard deviation of freeboard differences within 25 km bins for ON05. (d) Same as Figure 3c but for FM06. Standard deviations are computed for bins with more than two freeboard samples. *N* is the number of individual samples in Figures 3a and 3b and the number of bins in Figures 3c and 3d. The extent of the ice cover (in gray) is from AMSR ice products.

large volumes of ICESat data because of the need for visual inspection and the dependence on the availability of near coincident SAR image acquisitions. For our purposes, we acquired several hundred tiepoint estimates, H_{op}, using this approach for the assessment of the other two retrieval approaches described in this section.

[21] Figures 3a and 3b show the spatial distribution of mean H_{op} for the ON05 and FM06 periods. Each color-coded dot on the map represents the average of H_{op} estimates within 25-km grid cells (bins) defined on a polar stereographic projection. The histograms of standard deviation of H_{op} estimates within each 25-km bin are shown in Figures 3c and 3d; the means of the histograms provide an indication of the local temporal and spatial variability of H_{op}. The within-bin variability for both periods, at $\sim$3 cm, seems consistent and encouragingly small. In addition to the uncertainties due to noise in the ICESat elevations, the $\sim$3 cm standard deviation includes variability due to non-time-coincidence of the freeboard estimates. Even if the thicknesses within a 25-km bin are relatively homogeneous, variability associated with snow precipitation and ice growth is likely if time differences are large. At the basin scale, the spatial gradient in freeboard across the Arctic Ocean from north of Greenland to the Siberian Coast seems to be consistent with expectation but we shall return to this discussion in more detail in a later section.

[22] We find an interesting linear relationship between H_{op} and the 25-km standard deviation of detrended h_f', σ_{f-25} (see Figure 4). The samples are tightly distributed around the regression line with standard deviations of $\sim$2–3 cm. The regression slopes of 0.34 and 0.36 indicate that the expected freeboard is $\sim$3 times that of σ_{f-25}. This relationship is utilized in devising the two retrieval procedures that follow. Also, this linear relationship between elevation variation and mean is analogous to the relationship noted in the upward-looking sonar data between draft variation and draft mean [*Melling and Riedel*, 1996]. In the Beaufort Sea, they find that the mean draft is 1.15 of the draft standard deviation. We expect the top (freeboard) and bottom (draft) statistics to be similar but the difference in the proportionality factor is likely due to the difference in the reference level and perhaps the length scale under consideration. In our case, the reference level is chosen to be $\bar{h}_{25km}$ (a two-sided distribution) while in their case it is the actual sea surface (a one-sided distribution).

[23] To further examine this relationship, we compare the map of σ_{f-25} with the map of multiyear (MY) ice fraction derived from QuikSCAT (Figure 5). Since the higher

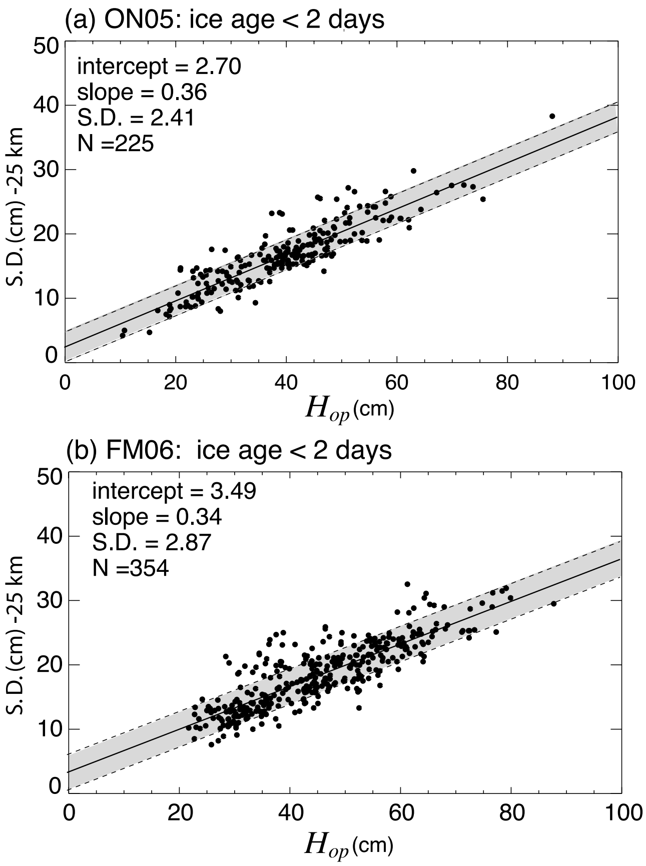

Figure 4. Relationship between freeboard from openings H_{op}(<2 days old) and the 25-km standard deviation of detrended elevation. (a) ON05. (b) FM06. The area covered by the $\pm 1\sigma$extent of the regression line is in gray.

fractions of MY ice coverage are areas of thicker ice, we expect a positive correspondence between the two spatial patterns; that is, high σ_{f-25} is correlated with high MY ice fraction. Indeed, we see a clear distinction in the values of σ_{f-25} between the regions with primarily seasonal ice (blue) and those with large fractions of MY ice (red). This seasonal ice zone stands out in the ON05 σ_{f-25} field (Figure 5d) because the ice is thinnest in the fall and consequently the freeboard is lowest. Compared to FM06, an expression of the thinner seasonal ice cover of the Arctic Ocean is also seen in the bimodal character of the ON05 σ_{f-25} distribution in Figure 5f. This provides further support of the relationship described above.

5.2. Low-Reflectivity ICESat Samples ($\delta h_{tp} = H_{\triangle R}$)

[24] Without the availability of SAR image sequences to establish the times of opening, we know only that dips along ICESat profiles contain samples of relatively thinner ice (but not necessarily centimeter level thin ice) and that sometimes these segments are also associated with dips in reflectivity, R (see Figure 2). Whether the reflectivity level is a useful parameter for identification of thin ice is conditional upon its relation to ice thickness and snow depth. Except for the rare occurrence of specular or quasi-specular returns (where $R > 1$) from very smooth water or ice surfaces, thin ice-filled leads (e.g., frazil, nilas, gray ice) have lower R than the adjacent snow covered sea ice or thicker ice [see *Kwok et al.*, 2006, Figure 11]. The reflectivity of bare ice increases only slowly with thickness. In contrast, the reflectivity of sea ice has a significantly stronger dependence on snow depth than thickness: a $\sim 1-2$ cm layer of snow completely masks the R of the underlying ice. If an open lead fills with a thin layer of snow shortly (hours to days) after opening, then the likelihood is high that low-reflectivity samples are new leads containing thin ice. In fact, *Kwok et al.* [2006] traced this rapid evolution in a 25-day ICESat reflectivity record of one aging lead in the high Arctic: they showed that the R of the lead samples increases from 0.25 to 0.5 within $\sim$2 days while the R of the adjacent ice cover (at around 0.7) remains nearly unchanged. After 5 days, the R of the lead becomes almost indistinguishable from that of the surrounding ice. Thus the combined dips in R and h_f' serve as effective indicators of young, thin ice in ICESat profiles.

[25] To show that there is a stable, basin-scale reflectivity in ICESat data, we plot the R-distributions of the ICESat samples of the sea ice cover from the two periods. Figure 6 shows that even though the values are uncorrected for atmospheric effects, the distributions from the two data sets have low scatter (standard deviations < 0.1) and are sharply peaked around the mean ($\bar{R}$ = 0.67 in ON05 and $\bar{R}$ = 0.66 in FM06) - an expression of the snow cover of Arctic sea ice. Snow reflectivity (or albedo) is generally lower at longer wavelengths (>800 nm) and lower than the spectrally averaged albedo. Compared to the model results of *Wiscombe and Warren* [1980], these mean values at the laser wavelength of 1064 nm are within the expected range considering the dependence of this parameter on snow grain size and shape, the possible effect of impurities (e.g., soot), and the mixture of ice type and surfaces.

[26] One way to demonstrate the effectiveness of combined dips in R and h_f' for identification of thin ice samples is to plot all h_f' with a reflectivity of 0.3 lower than that of the surrounding snow covered ice (i.e., $\Delta R > 0.3$) against the detrended standard deviation, σ_{f-25}, defined above (Figure 7). Here $\Delta R = R_{bg} - R$ and R_{bg} is the local background reflectivity. At each laser shot, R_{bg} is taken as the average reflectivity of all the samples within a 25-km segment (centered at that sample) that are greater than $\bar{R} - 1.5\sigma$. This threshold serves to exclude the low-reflectivity samples of open leads from entering into the calculation of R_{bg}. Figure 7 shows that all samples with $\Delta R > 0.3$ have a linear relationship between σ_{f-25} and h_f' similar to that shown in Figure 4. It is also interesting to note that the distribution of h_f' with $\Delta R > 0.3$ is distinctly bimodal in the fall (ON05) with one mode at a lower mean h_f' that is characteristic of the large region of seasonal ice as well as a thicker mode indicative of MY ice. In the winter FM06 distribution, this mode is less apparent and seems to have merged with the mode of the thicker ice. To show where the distributions of new openings from Figure 4 lie in Figures 7a and 7b, we superimpose the areas (in gray) that are defined by the $\pm\sigma$ extent of the regression lines from Figures 4a and 4b. It is clear from these results that while only a fraction of these samples are new openings as defined in section 5.1, the results in Figure 4 delineate the regions within which the samples of thinnest ice are most likely to be found. In our retrieval process, we select all samples with

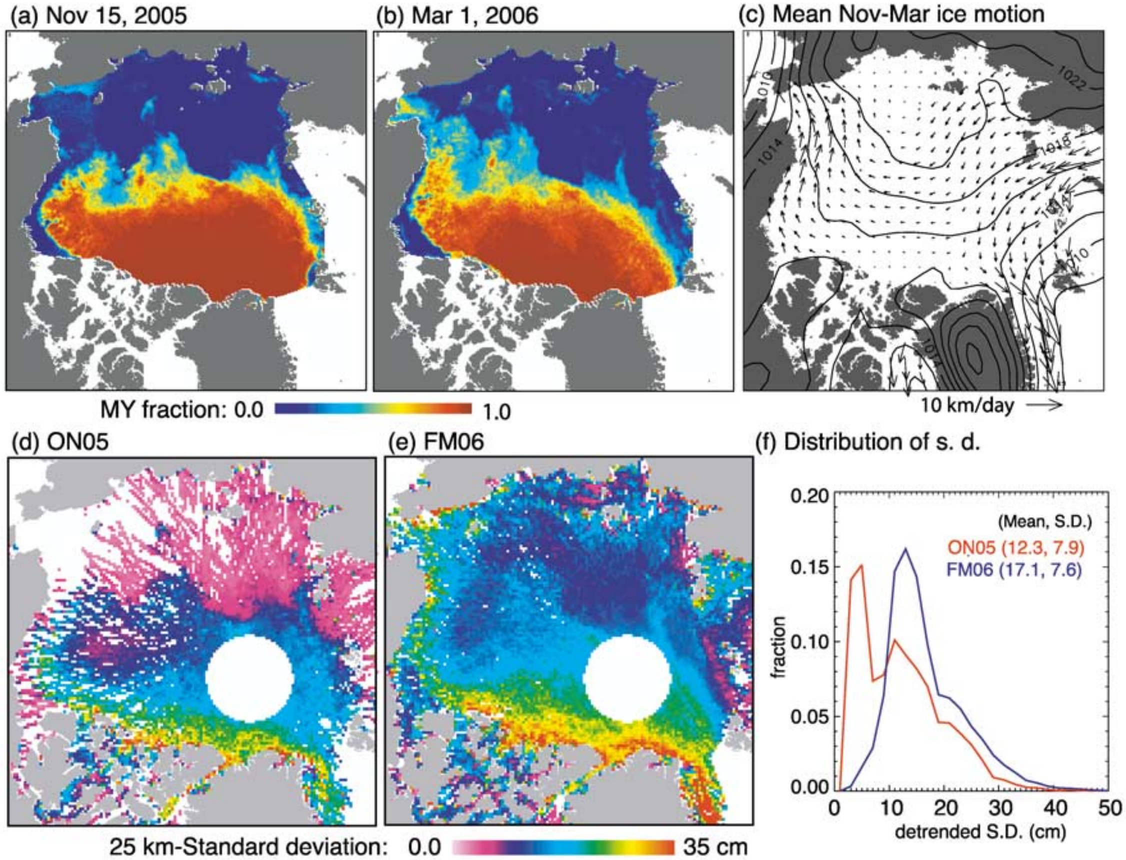

Figure 5. QuikSCAT multiyear (MY) ice fraction and standard deviation of detrended ICESat elevation. (a) QuikSCAT MY ice fraction, 15 November 2005. (b) QuikSCAT MY ice fraction, 1 March 2006. (c) Mean November–March ice motion from passive microwave data. (d) Standard deviation of detrended ICESat elevation profile: ON05. (e) Standard deviation of detrended ICESat elevation profile: FM06. (f) Distribution of standard deviation in ON05 and FM06.

$\Delta R > 0.3$ that are located below the mean regression line (bold line in Figure 7) to be suitable for use as sea surface reference. We designate the sea surface estimates retrieved with this approach as $H_{\Delta R}$.

[27] In the following, contiguous estimates of $H_{\Delta R}$ are assumed to be from the same lead and considered correlated, and thus provide only a single independent measurement of sea level. This process retrieved only 3848 and 7681 ICESat independent sea surface segments in the ON05 and FM06 data sets. These are very small numbers compared to the $\sim 2.3 \times 10^6$ and 4.8×10^6 ICESat elevation samples from the two seasons. Physically, this suggests that a thin covering of snow or frost flowers [*Martin et al.*, 1995] obscures the natural reflectivity of a significant number of young leads and that narrower leads of low reflectivity are not resolved by the ICESat footprint.

[28] Since H_{op} from near coincident ICESat/SAR data are clearly our best available estimates, we can assess the quality of the retrieved sea surface obtained with this procedure by comparison of estimates of $H_{\Delta R}$ with that of H_{op} (Figures 8a and 8d) that are within 12.5 km of each other. So that the estimates are independent, the H_{op} tiepoints have been removed from the list of $H_{\Delta R}$ tiepoints. The plots show the mean differences and scatter between

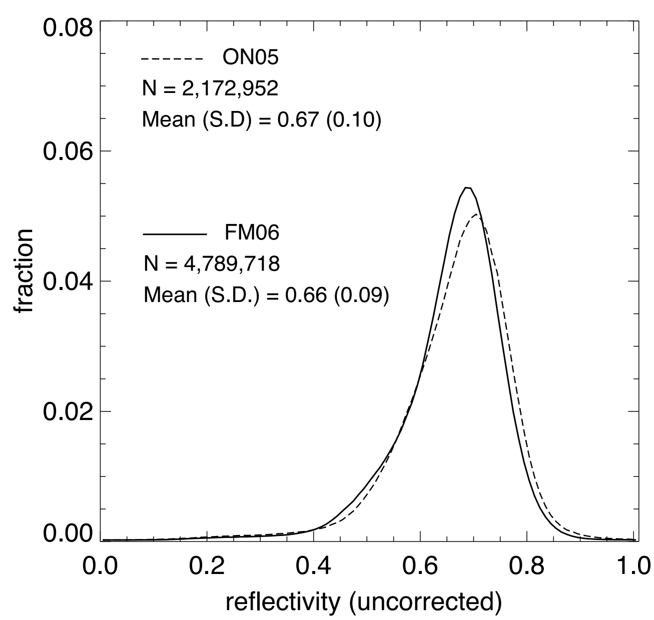

Figure 6. Distribution of uncorrected ICESat reflectivity in ON05 and FM06. *N* is the number of ICESat samples.

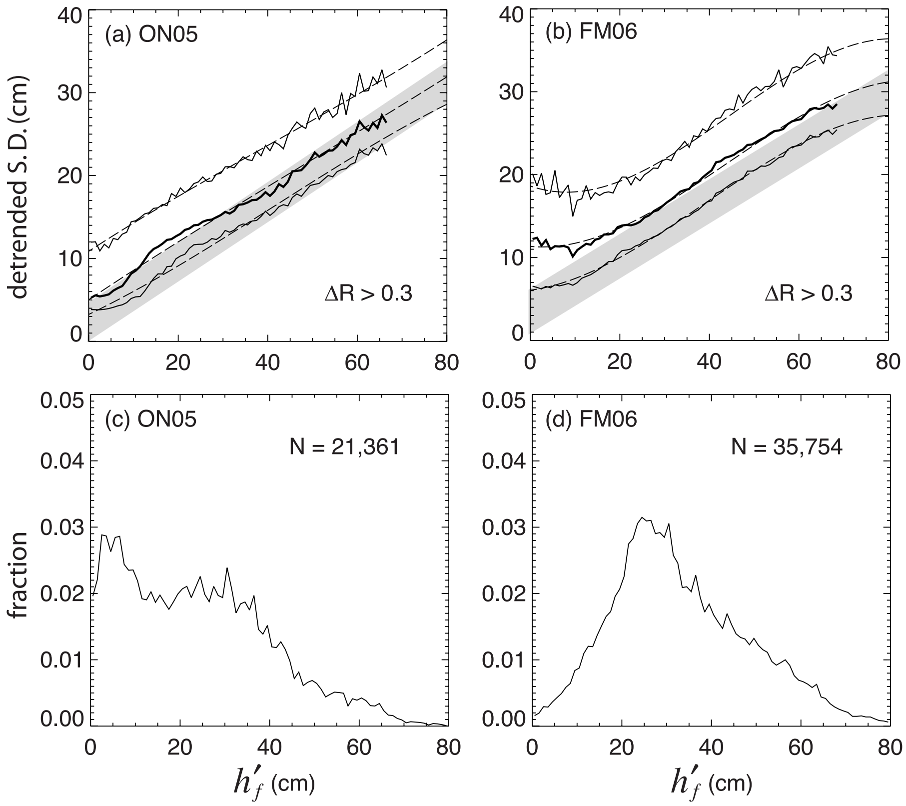

Figure 7. Relationship between detrended standard deviation of elevation σ_{f-25} and h'_f of samples with $\Delta R > 0.3$. (a) ON05. (b) FM06. The lines connect the mean (in bold) and ± rms values of ICESat samples within 1-cm bins. Their associated regression lines, cubic polynomial fits, are dashed. The gray areas in Figures 7a and 7b are the regions enclosed by the $\pm 1\sigma$ extent of the regression lines in Figures 4a and 4b, respectively. They show expected relationship between σ_{f-25} and the freeboard of new openings. (c) Distribution of h'_f : ON05. (d) Distribution of : FM06.

the tiepoints from the two approaches to be quite small: −1.6 ± 4.8 cm in ON05 and −4.0 ± 5.6 cm in FM06. The difference shows that in the mean $H_{op} > H_{\Delta R}$. This is consistent with our expectation: the $H_{\Delta R}$ samples do not always contain the thinnest ice even though they satisfy the conditions set forth above. Overall, the comparison demonstrates that, for both seasons, this retrieval approach provides reasonably good sea surface tiepoints, though slightly underestimated by up to 4 cm.

5.3. Relation Between Sea Surface Level and Standard Deviation of ICESat Elevation ($\delta h_{tp} = H\sigma$)

[29] Another set of sea surface estimates can be obtained by selecting all samples below the mean regression line (bold line in Figure 7) without the additional requirement of having a concomitant dip in reflectivity. This approach selects all samples of h'_f that are greater than $\beta \bullet \sigma_{f-25}$, where β is the reciprocal of the slope of the lines shown in Figure 4. The value of β is ∼3. If h'_f were normally distributed, then only ∼0.5% of the samples are expected to contain thin ice or elevations that are close to the local sea surface. The smaller value of β in ON05 ($\beta = 2.8$) compared to that in FM06 ($\beta = 3$) could be fortuitous, but the slight difference does make sense since there would be a higher percentage of near sea surface samples or young leads during the fall. Interestingly, the value of 0.5% also corresponds to the expected fractional area of young openings as measured by SAR ice motion [*Kwok*, 2002].

[30] Similarly, we can assess the quality of these freeboard estimates (designated H_σ) by comparing them with available $H_{\Delta R}$ and H_{op} that are within 12.5 km of H_σ. As above, the H_{op} tiepoints have been removed from the list of H_σ tiepoints. Likewise, $H_{\Delta R}$ tiepoints have been removed from the list of H_σ tiepoints. The results are shown in Figures 8b, 8c, 8e, and 8f. The mean difference shows that $H_{op} > H_\sigma$. This is again consistent with our expectation that this approach underestimates the value of local freeboard/sea surface since the selected tiepoints do not always contain the thinnest ice. The mean difference between H_{op} and H_σ (at −1.3 ± 5.6 cm in ON05 and −3.1 ± 5.8 cm in FM06) indicates that this retrieval approach provides slightly lower quality sea surface estimates than that obtained above. The scatter is comparable to the previous approach. With a much larger sample size, the differences between $H_{\Delta R}$ and H_σ are similar for both seasons. Without the reflectivity dip requirement, some of the samples may contain snow/frost flower covered leads (with variable depths) that increase the local snow/ice thicknesses and effectively bias the local sea surface estimates. The merit of this approach is that it identifies more than six times the

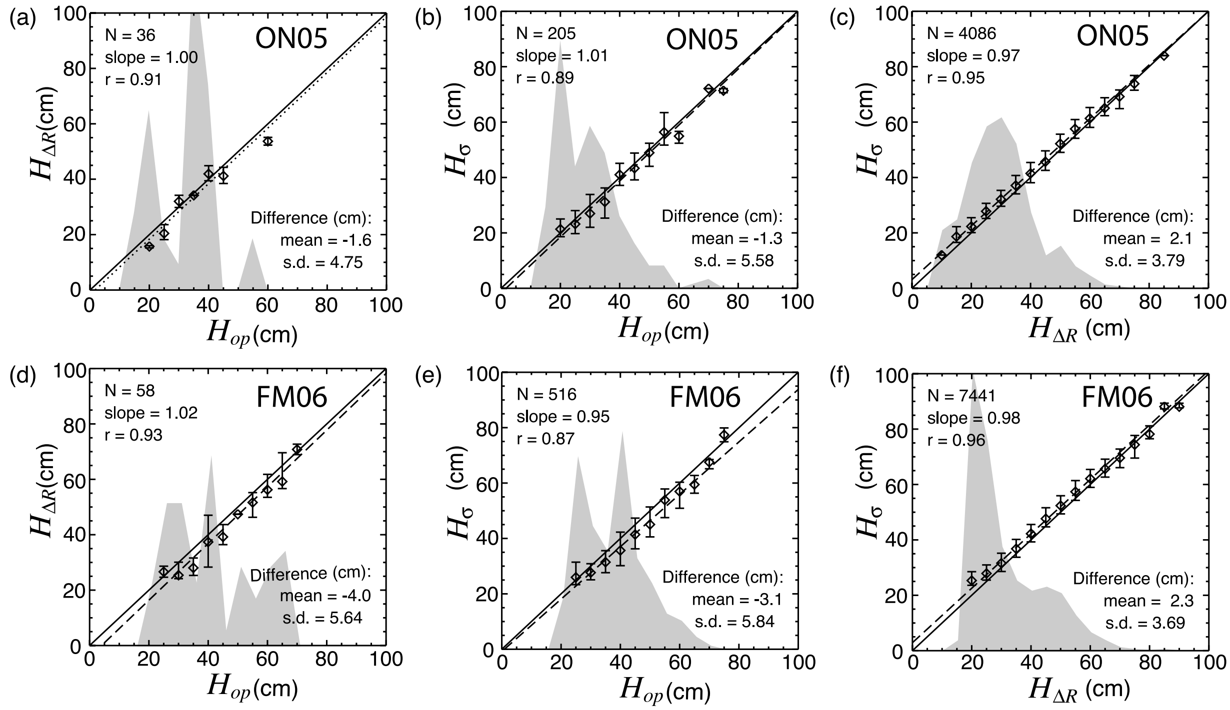

Figure 8. Comparisons of retrieved freeboards (H_{op}, $H_{\Delta R}$ and H_σ) from the three approaches for $\Delta R >$ 0.3 and for h_f' below the regression line in Figure 7. (a) $H_{\Delta R}$ versus H_{op} in ON05. (b) H_σ versus H_{op} in ON05. (c) H_σ versus $H_{\Delta R}$ in ON05. (d) $H_{\Delta R}$ versus H_{op} in FM06. (e) H_σ versus H_{op} in FM06. (f) H_σ versus $H_{\Delta R}$ in FM06. Histograms (in gray) show the relative freeboard distribution of the sample populations.

number of sea surface segments (25410 in ON05 and 45109 in FM06), albeit at a lower quality, compared to the previous approach.

6. Seasonal Variability of Sea Ice Freeboard

[31] The previous section outlines three sea surface retrieval approaches that provide results with different levels of uncertainty. The new openings identified in ICESat/SAR data provide the best sea surface reference, while the two estimates that are derived exclusively from ICESat data are of lower quality. However, the strength of the latter two approaches is that they provide a denser sampling of the local sea surface for freeboard estimates throughout the Arctic basin. Thus one could select the retrieval approach on the basis of whether one's interest is local or regional. In this section, we describe a procedure for combining these estimates that allow us to construct freeboard maps for examining their spatial and seasonal variability over the Arctic Ocean. Extensive assessments of the freeboard estimates could only be qualitative at this time but the internal consistency of the estimates in time and space, as we demonstrate below, show that they at least satisfy the expected seasonal constraints.

6.1. Sea Surface Estimates Along 25-km Segments

[32] To combine tiepoint estimates within ICESat segments, we first examine the quality of the retrieved tiepoints $H_{\Delta R}$ and H_σ by characterizing their differences with H_{op} for $\Delta R > 0.4$ and $\Delta R > 0.5$, and for tiepoints that are more than 0.5σ below the regression line instead of just below the line. The comparisons in Figure 9 show that, for both the ON05 and FM06 periods, their differences are reduced (i.e., closer to zero) for larger ΔRs and for tiepoints that are farther below the regression line. Since the tendency of the tiepoints is toward an underestimation of the freeboard (Figures 8 and 9) when compared to H_{op}, this motivates a weighting function that assigns the highest weight to points with larger $H_{\Delta R}$ or H_σ, or to those that are farthest from the line. Within 25-km segments, we combine $H_{\Delta R}$ and H_σ by exponentially weighting their distance from the mean regression line in Figure 7 as follows:

$$\partial \hat{h}_{tp} = \sum_i \alpha_i H^i_{\Delta R} + \sum_j \beta_j H^j_\sigma, \tag{8}$$

where α and β are the normalized weights. Each 25-km segment contains ~150 individual ICESat elevation samples. The weighting of each estimate is e^{2d/σ_r}: $\frac{d}{\sigma_r}$ is the normalized distance (scaled by the standard deviation) of the point from the line. With the estimate $\partial \hat{h}_{tp}$, the pointwise freeboard is then calculated via equation (6): $\hat{h}_f = \delta \hat{h}_{tp} - h_f'$.

[33] The expected uncertainties in sea surface retrieval depend on the quality of the tiepoints within each 25-km segment. Here we restate the approximate uncertainties for the two categories of tiepoints, they are: -1.6 ± 4.8 cm in ON05 and -4.0 ± 5.6 cm in FM06 for $H_{\Delta R}$, -1.3 ± 5.6 cm in ON05 and -3.1 ± 5.8 cm in FM06 for H_σ. On the basis of these statistics, when the tiepoints are combined using equation (8), we expect the sea surface estimates to be slightly biased (which lowers the freeboard) and the uncer-

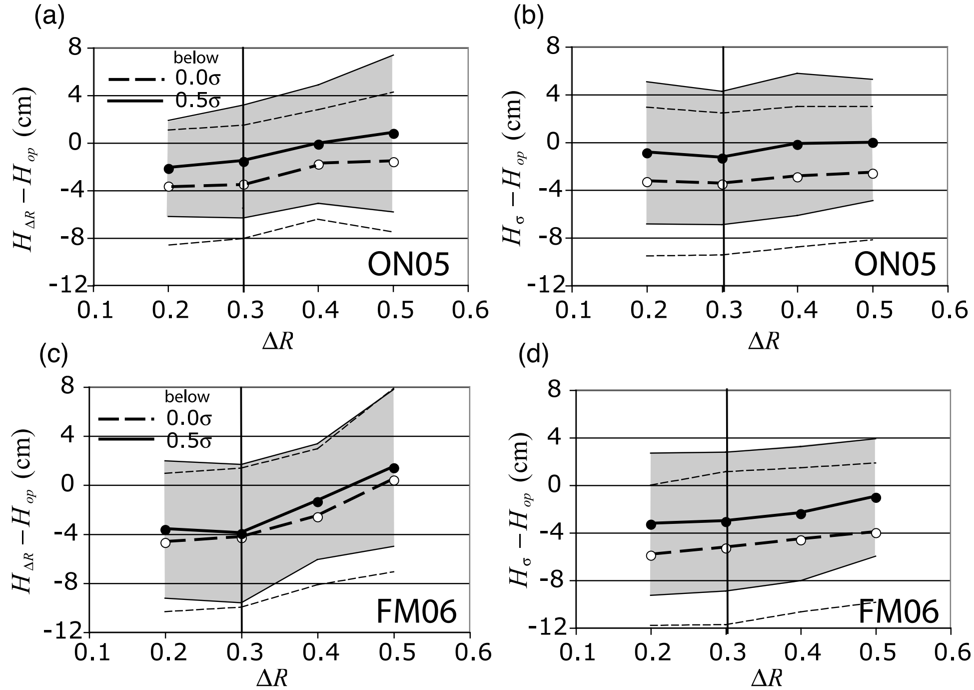

Figure 9. Dependence of the quality of retrieved tiepoints, $H_{\Delta R}$ and H_σ, on ΔR and distance from regression line. (a) $H_{\Delta R} - H_{op}$ in ON05. (b) $H_\sigma - H_{op}$ in ON06. (c) $H_{\Delta R} - H_{op}$ in FM06. (d) $H_\sigma - H_{op}$ in FM06. Dashed lines connect the mean (open circles) and standard deviation for samples that are below the regression line. Solid lines connect the mean (solid circles) and standard deviation for samples that are 0.5 σ below the regression line.

tainties to be ~6 cm or better. However, the final uncertainty is ultimately dependent on the number of tiepoints available. We note here that the $\partial\hat{h}_{tp}$ estimate is used only within each nonoverlapping 25-km segment. The information is not extrapolated to adjacent segments and freeboard estimates are not produced for segments with no tiepoints. For the two periods here, the average number of tiepoints in all segments with at least one tiepoint is ~3.9. Typically, tiepoints are not uniformly distributed in space; they are usually concentrated regionally. This can be attributed the response of the ice cover to atmospheric forcing: the spatial distribution of leads is not uniform and a system of open leads is usually associated with the passing of a storm.

6.2. Spatial Pattern of Freeboard Composites

[34] Figure 10 shows the maps of retrieved freeboards from the ON05 and FM06 seasons on a 25-km grid. The value of each cell represents the mean freeboard (Figure 10a) of all 25-km segments that fall within its geographic bounds. The standard deviation maps (Figure 10b) are created similarly. Only 25-km segments that contain sea surface estimates are used in the construction of these maps; others are not plotted. The right-hand plots of Figures 10 and 10b show the histograms of mean and standard deviation of the retrieved freeboard of the maps and the total number of grid cells with freeboard estimates.

[35] Broadly, the fall (ON05) map shows an extensive region of seasonal ice of very low freeboard (0−15 cm, magenta) that occupies a large fraction of the Arctic Ocean. It covers the southern Beaufort Sea, the Chukchi, East Siberian and Laptev Seas and extends as far north as 80°N. The highest freeboards (up to 80 cm) can be found in the ice cover north of Ellesmere Island, Greenland, and in the Lincoln Sea. The mean and S.D. of the gridded freeboards during this period is 27.5 ± 15.5 cm. As expected, the winter (FM06) map shows much higher overall freeboard. The magenta colored areas in the fall map is no longer present. As a result of ice growth and snow accumulation, the lowest freeboards in the seasonal ice zone are now over 15 cm (blue) and there are larger areas of higher freeboard (red, yellow and light blue) compared to the fall map. The increase in the mean freeboard is 7.5 cm.

[36] While the mean freeboard distributions during the fall (ON05) and winter (FM06) satisfy our expectation of freeboard increases during the ice growth season, the S.D. maps and histograms are telling of the consistencies in freeboard retrieval. The S.D. is a measure of the sub-grid-scale variability of the retrieved freeboards. Potential sources of variability are: (1) natural variability of the sea ice freeboard in space and time: the data are acquired during two ~35 day periods; and (2) uncertainties introduced in the freeboard retrieval process. The S.D.s are ~3 cm in both the fall and winter data sets. These values are encouragingly small. Since these distributions do not seem to depend on season, they increase our confidence in the consistency of our retrieval approaches. The higher variability around the data hole is most likely due to the larger number of samples due to converging orbits and thus higher temporal separation and differences between subgrid samples.

6.3. Freeboard of First-Year and Multiyear Sea Ice (25-km Grids)

[37] One complicating factor in assessing the seasonal freeboard differences is the varying spatial coverage of MY

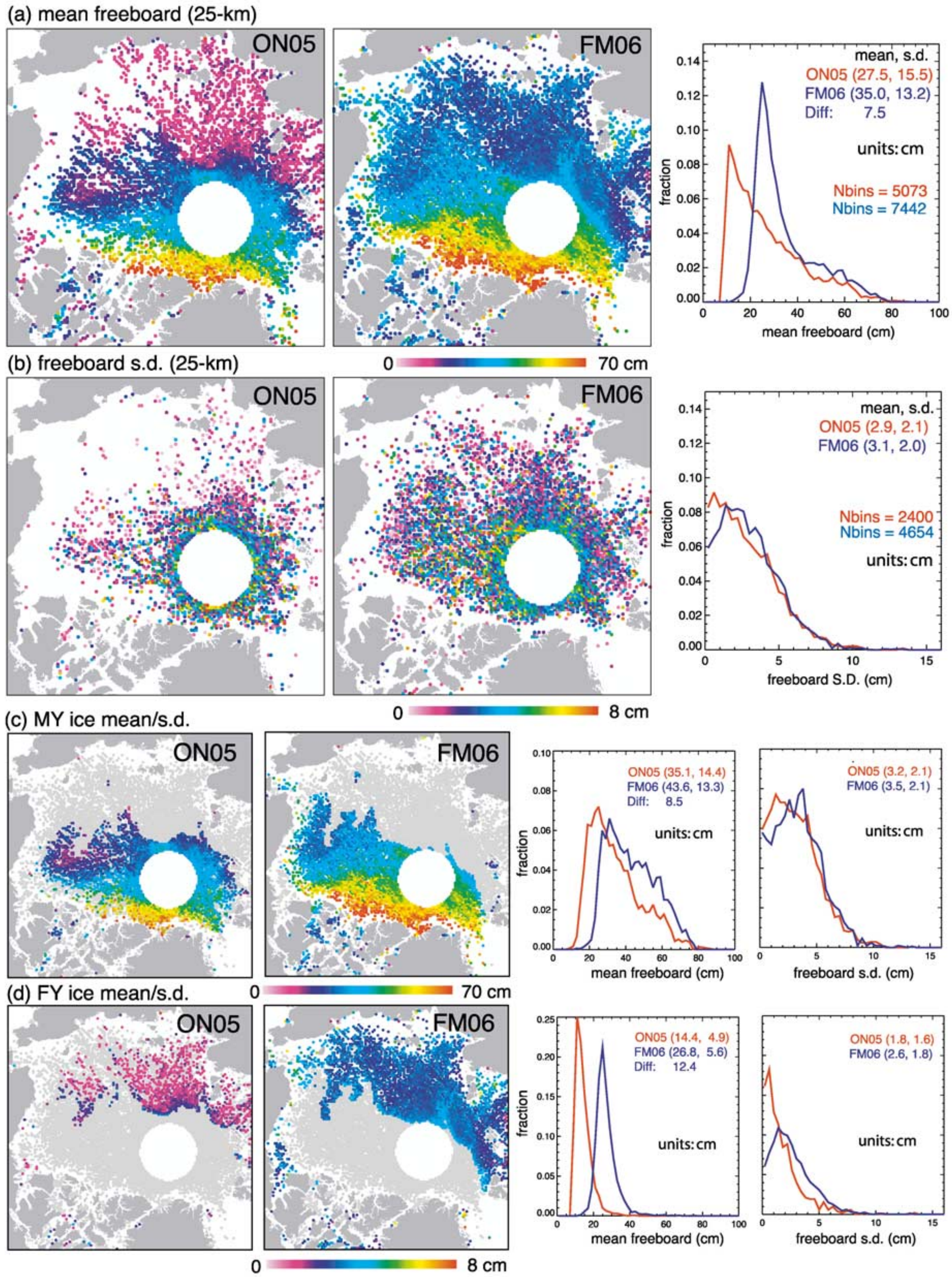

Figure 10. Maps of retrieved freeboards (25 km bins) from the ON05 and FM06 ICESat data set. (a) Mean freeboard. (b) Standard deviation. (c) Mean and standard deviation of freeboard in multiyear ice region (>80% MY concentration). (d) Mean and standard deviation of freeboard in first-year ice region (<80% MY concentration). MY fraction masks are derived from the QuikSCAT fields shown in Figure 4.

ice due to advection. Even as a broad measure of the seasonal changes, a simple spatial difference between the freeboard fields would mix FY and MY samples and give unrealistically large differences when the effects of ice motion is not considered. In our assessment of these fields, we first separate the FY and MY samples with spatial masks of the two primary ice types derived from the maps of MY fraction in Figures 5a and 5b. To examine only the freeboard changes over the MY ice cover, all grid cells with less than 0.8 MY fraction are masked out (Figure 8c). Conversely, for examination of changes in the freeboard of the FY ice cover only grid cells with MY fractions of less than 0.8 are included (Figure 8d). The associated freeboard distributions of the FY and MY ice covers are shown in the right panels of Figures 10c and 10d. The choice of 0.8 MY fraction isopleth for delineating the ice zones is quite arbitrary: since the spatial gradient in MY fraction near the edge of the MY and FY ice zones is high, changing the threshold does not move the boundaries or the coverage of each ice type significantly.

[38] The increase in the mean freeboard of the MY sea ice cover between ON05 and FM06 is 8.5 cm, starting with a mean of ~35.1 cm in ON05. In ON05, the mean freeboard of the seasonal ice cover is only 14.4 cm but the increase in freeboard (12.4 cm) over the ~4 months is higher over the FY ice cover. The FY ice cover has a larger increase in mean freeboard due to the more rapid growth of seasonal ice during the fall, even though the contribution of snow accumulation to freeboard may have started at a later date compared to that over the existing MY ice cover. In addition, the freeboard distributions of the seasonal ice cover (with S.D.s of ~5 cm) are sharply peaked in both the fall and winter; this can be attributed to the fact that the seasonal ice cover is formed quite quickly at end of summer and therefore the samples have similar ice age. The higher variability in the age and deformation of the MY ice cover contributes to its larger S.D. (of ~15 cm).

6.4. Differences in Regional Freeboard Distributions

[39] Rather than the low-resolution gridded fields, the finer-scale freeboard distributions shown in Figure 11 can be examined. Each distribution is constructed using the freeboard estimates of individual ICESat samples (~70-m spots) from 25-km segments that contain sea surface references. Each square in Figure 11 is 700 km on a side. For each region, we show: (1) the number of 25-km segments with sea surface references compared to the total within the box; (2) the mean and standard deviation of the distributions; and (3) the percentage of samples with negative freeboard and their mean deviation from the estimated sea surface.

[40] First we discuss the negative freeboard. There is a small fraction of samples within a collection of 25-km segments that have negative freeboards, i.e., below the sea surface. Since the sea surface retrievals and the ICESat elevations are noisy, it is expected that we have negative values: over relative smooth surfaces, the precision (or noise) of the ICESat elevations is ~2 cm [*Kwok et al.*, 2006]; and, the sea surface retrieval approaches do not necessarily identify samples with the most extreme h_f' to be sea surface references. Additionally, there are residuals in sea surface heights, h_{ssh}', that are not captured by $\bar{h}_{25km}$. All these factors contribute to negative freeboards. Overall, they represent less than 1% of the samples and on average they are less than 1.5 cm below the estimated sea surface; these values are within expected bounds.

[41] Again, the sharply peaked distributions of the seasonal ice cover during both the fall and winter stand out. Freeboard extremes in the ON05 range from the region over the East Siberian Shelf (11.4 cm) to north of the Greenland Coast (50.7 cm). Similarly, the lowest freeboard in FM06 can be found just east of the New Siberian Islands (24.9 cm) while the highest freeboard remains just north of Greenland (55.5 cm). The longer tails and higher S.D. in the distributions with higher freeboard (thicker ice) are due to ridges and deformed ice.

[42] Figure 12 contrasts the freeboard distributions and shows their mean differences between ON05 and FM06 retrievals. These differences are expressions of regional changes in freeboard due to snow accumulation, ice growth, and ice advection. The changes in freeboard are generally higher in the seasonal ice zone (an increase of 17.2 cm just north of Alaska) and lower over the MY ice cover in the central Arctic and north of Greenland. The rate of ice growth, as mentioned earlier, is highest in the thinner seasonal ice and probably the largest contributor to the increase in freeboard. Over MY ice, the differences are more moderate and can be compared to the expected changes in the Arctic Ocean mean snow depth of 9 cm between the end of October and end of February [*Warren et al.*, 1999].

6.5. Comparison of Freeboard Estimates: ICESat and Ice Mass Balance Buoys

[43] There are no direct freeboard measurements at the ICEsat length scale for assessment of the estimates obtained here. However, current ice mass balance buoys (IMBs) that are deployed on Arctic sea ice report both ice thickness and snow depth, and these could be converted to freeboard for comparison purposes. On these buoys, an above ice acoustic rangefinder measures distance between the instrument and the snow surface to record the changes in snow depth. Similarly, bottom growth and ablation are from an under-ice acoustic rangefinder that measures distance between the instrument and the ice bottom. Data are sent through the ARGOS satellite system using on-buoy transmitters. A description of the IMB instrumentation and data sets can be found available on the website http://www.crrel.usace.army.mil/sid/IMB/in dex.htm. The processed data are sampled on a 2-hourly basis.

[44] As the IMBs do not measure freeboard directly, the first step is to convert the available ice thickness and snow depth data to freeboard $h_{freeboard}$. Assuming hydrostatic equilibrium,

$$h_{freeboard} = \frac{(\rho_w - \rho_i)}{\rho_w} h_{ice} + \frac{(\rho_w - \rho_s)}{\rho_w} h_{snow}. \tag{9}$$

In addition to the thicknesses of ice (h_{ice}) and snow (h_{snow}), the freeboard is dependent on their respective densities. The density of seawater, ρ_w, is assumed to be constant (1024 kg/m^3) and the snow bulk density, ρ_i, is assumed to follow the seasonal dependence of *Warren et al.* [1999]. We compute

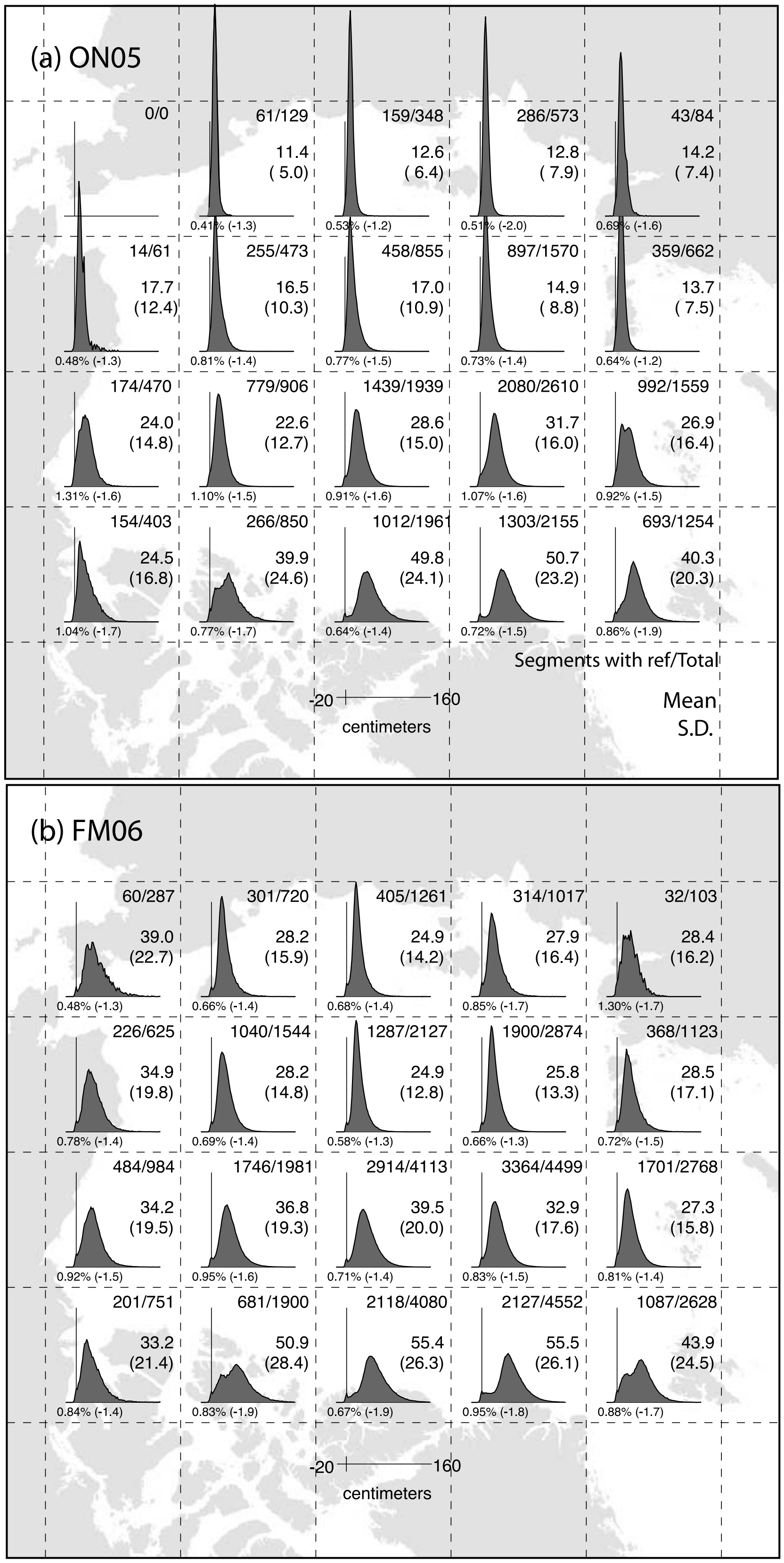

Figure 11. Freeboard distributions. (a) ON05. (b) FM06. Distributions are of individual samples from 25 km segments with each 700 km by 700 km region. Only segments with at least one sea surface reference are used. For each region, the following are shown: (1) the number of these segments with sea surface reference compared to the total; (2) the mean and standard deviation of the distributions; and (3) the percentage of samples with negative freeboard and their mean deviation from the estimated sea surface.

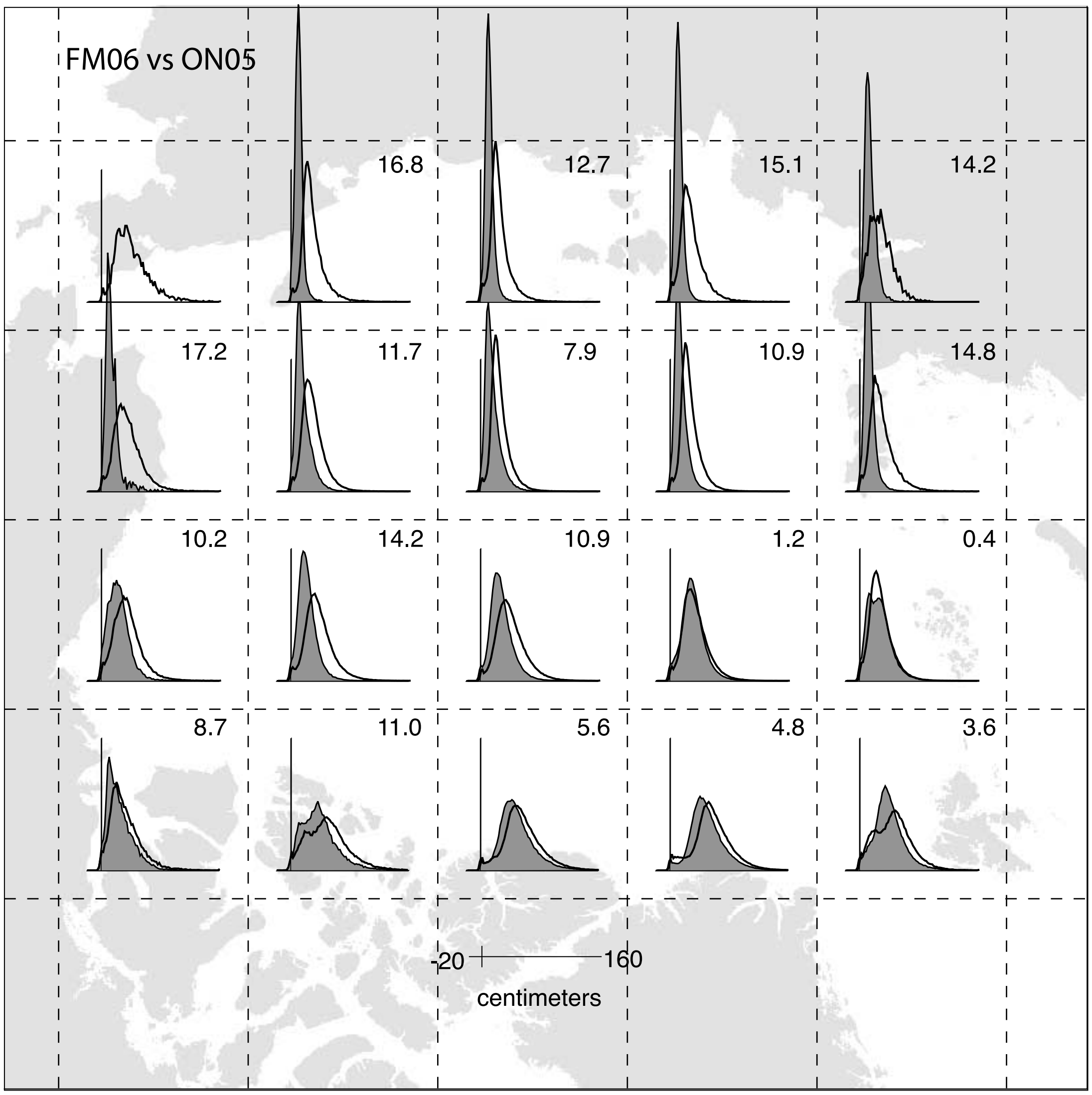

Figure 12. Differences between the freeboard distributions from ON05 and FM06. The difference in the mean freeboard (in centimeters) is shown in the top right corner of each box.

sea ice bulk density, ρ_i, in two ways. The first approach uses the thickness-dependent parameterization of *Kovacs* [1996],

$$\rho_i = 0.9363 - 0.0018 h_{ice}^{0.5} \quad \left(g/cm^3\right). \tag{10}$$

The above equation is derived from measurements of ice cores from the Beaufort Sea and shows that the bulk density decreases with ice thickness. For first-year sea ice, the decrease is associated with brine drainage and growth rate processes, which reduce the volume fraction of the heavier brine entrained within the ice. The lower multiyear ice densities are the result of the inclusion of proportionally less brine and more gas, especially in the freeboard portion, which is nearly low-density fresh ice. In the conversion to ice freeboard, the uncertainty in bulk density is a significant source of error as it varies by over 15% between 1 m and 3 m thickness. In the second approach, we use a mean density and vary it over a range, i.e., $\rho_i = 0.915 \pm 0.01$ g/cm^3 [*Weeks and Lee*, 1958; *Schwarz and Weeks*, 1977].

[45] The comparisons are shown in Table 1. During the period of interest, the rangefinders on one of the four buoys failed and Buoy 7498 recorded data only during the fall. All three buoys are located on MY sea ice and their drift tracks are shown in Figure 13. Buoy 25752 was inside the ICESat data hole and the freeboard estimates are from the nearest neighborhood ICESat samples. The IMB snow depth and ice thickness estimates represent 30-day averages spanning approximately the same time period as the ICESat data sets. The ICESat freeboards are from the fields shown in Figure 10; each estimate provides a mean value and the expected variability at that grid location.

[46] First, the ICESat freeboards and those derived from Buoys 25752 and 7948 show reasonably good agreement in terms of absolute freeboard and their changes over the 4-month period; the freeboards are within several centimeters of each other. These results seem quite remarkable considering the ICESat estimates are on a fairly coarse spatial scale while the IMBs provide point measurements. Perhaps these results are not as surprising after considering that the

Table 1. Comparison of Freeboard From ICESat With Those Derived From Ice Mass Balance Buoys[a]

	ICESat Freeboard		IMB					ICESat-IMB		
			Snow	Ice	Freeboard[b]	Freeboard[c]		Freeboard[b]	Freeboard[c]	Comments
Buoy 25752										interpolated ∼ 200 km
ON05	33.7	(5.2)	8.9	261.0	267.4	34.2	(2.5)	−233.7	−0.5	
FM06	45.8	(3.9)	18.2	295.0	307.5	43.9	(2.9)	−261.7	1.9	
Change	12.1		9.3	34.0	40.1	9.8		−28.0	2.3	
Buoy 7948										
ON05	29.0	(4.1)	21.0	171.0	186.1	33.3	(1.7)	−157.1	−4.3	
Buoy 7950										hummocky area
ON05	28.0	(7.8)	3.0	321.0	323.2	36.3	(3.5)	−295.2	−8.3	
FM06	42.0	(9.3)	16.0	354.0	365.0	48.7	(3.1)	−323.0	−6.7	
Change	14.0		13.0	33.0	41.8	12.4		−27.8	1.6	

[a]IMB denotes ice mass balance. Units are centimeters. Standard deviations are in brackets.
[b]Sea ice bulk density is $\rho_i = 0.9363 - 0.0018 h_i^{0.5}$ g cm^{-3}.
[c]Sea ice bulk density is $\rho_i = 0.915 \pm 0.01$ g cm^{-3}.

errors in freeboard are multiplied tenfold in the conversion to errors in ice thickness. Another source of variability is the expected spatial variability of ice thickness and snow depth over the Arctic ice cover. Thus the level of agreement could be entirely fortuitous. On one hand if the placement of these buoys is on relatively level MY ice, the measured ice thickness and snow cover could be expected to be somewhat closer to the larger-scale average. On the other, it would also imply fairly long spatial correlation length scales (tens of kilometers) in the freeboard or the snow depth and ice thickness; certainly the IMBs are not sensitive to changes in freeboard associated with local ice dynamics. Also, the freeboard fields in Figure 8 do seem to have fairly long correlation length scales.

[47] Second, the derived freeboard from Buoy 7950 highlights the sensitivity of the estimates to sea ice bulk density. The larger differences at Buoy 7950 may be attributed to its location in a hummocky area as evidenced by a thinner snow cover during the fall and winter. In addition, the thickness-dependent parameterization of *Kovacs* [1996] predicts that the bulk density of the ∼3.5 m ice to be ∼0.903 g/cm^3 thus giving a freeboard that is much higher when compared to the ICESat estimates. While the comparisons seem more reasonable when the mean bulk density is used, it is not clear which of the two provides a better assessment of the ICESat freeboards. Unfortunately, a better understanding of the spatial and seasonal variability of the sea ice bulk density is lacking. This underscores the importance of such characterizations in the conversion of freeboard to thickness and vice versa.

[48] Third, it is interesting to note (from the IMB measurements) that changes in snow depth account for 90% of the increase in freeboard between late October and late February. Also, since these changes are relatively independent of sea ice density (especially in slow growth areas), the uncertainties in these changes should be smaller. Indeed, the comparisons show that the seasonal differences in freeboard (∼2−3 cm) are in better agreement with each other than the absolute freeboard estimates. It seems that seasonal changes in ICESat freeboard over old ice provide good estimates of changes in snow depth.

[49] Last, though the number of data points used in this comparison is small, it serves to illustrate that a few well-placed buoys could go a long way for the validation of ICESat sea ice freeboard retrievals if it could be demonstrated, with a larger data set, that point measurements from IMBs are indeed useful after considering the issues discussed above.

7. Residual Sea Surface Height

[50] The sea surface level is another parameter that allows us to assess the consistency in our retrieval approach. By subtracting out the sea ice freeboard, we can compute the residual sea level as follows:

$$h_{res} = h'_{ssh} - \hat{h}_{ssh} = \bar{h}_{25km} - \delta h_{tp}. \tag{11}$$

This residual does not include the modeled portion of the sea surface height (i.e., $\hat{h}_{ssh}$ as described earlier) but includes all the unexplained static and time-varying components of the sea surface as well as noise introduced by our estimation process. It is a crude measure of $\tilde{h}_{ssh}$, the errors in estimating of sea surface height.

[51] The fields of h_{res} on a 25-km grid are shown in Figure 14. The difference field (Δh_{res}) and the distributions of the mean and difference fields are also shown. The results show that the two distributions share approximately the same mean and standard deviation: 26.7 ± 22.2 cm in ON05 and 26.2 ± 23.3 cm in FM06. The difference statistics at −1.8 ± 14.2 cm shows a negligible mean and a reduced standard deviation.

[52] There is a mean level for both fields that differ by ∼2 cm. Their standard deviations indicate that the variability of the estimates is similar. The ON05 and FM06 fields have correlated spatial structures while a more random

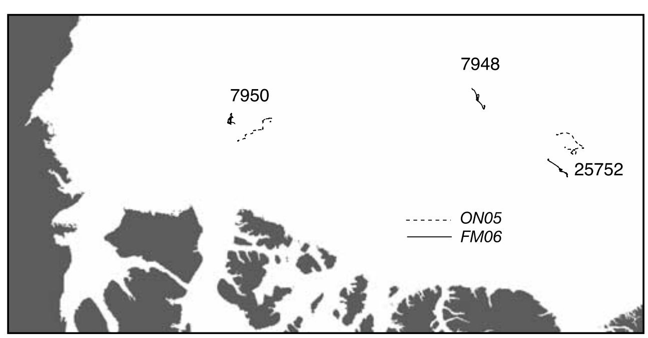

Figure 13. Drift tracks of the ice mass balance buoys in ON05 (dashed lines) and FM06 (solid lines).

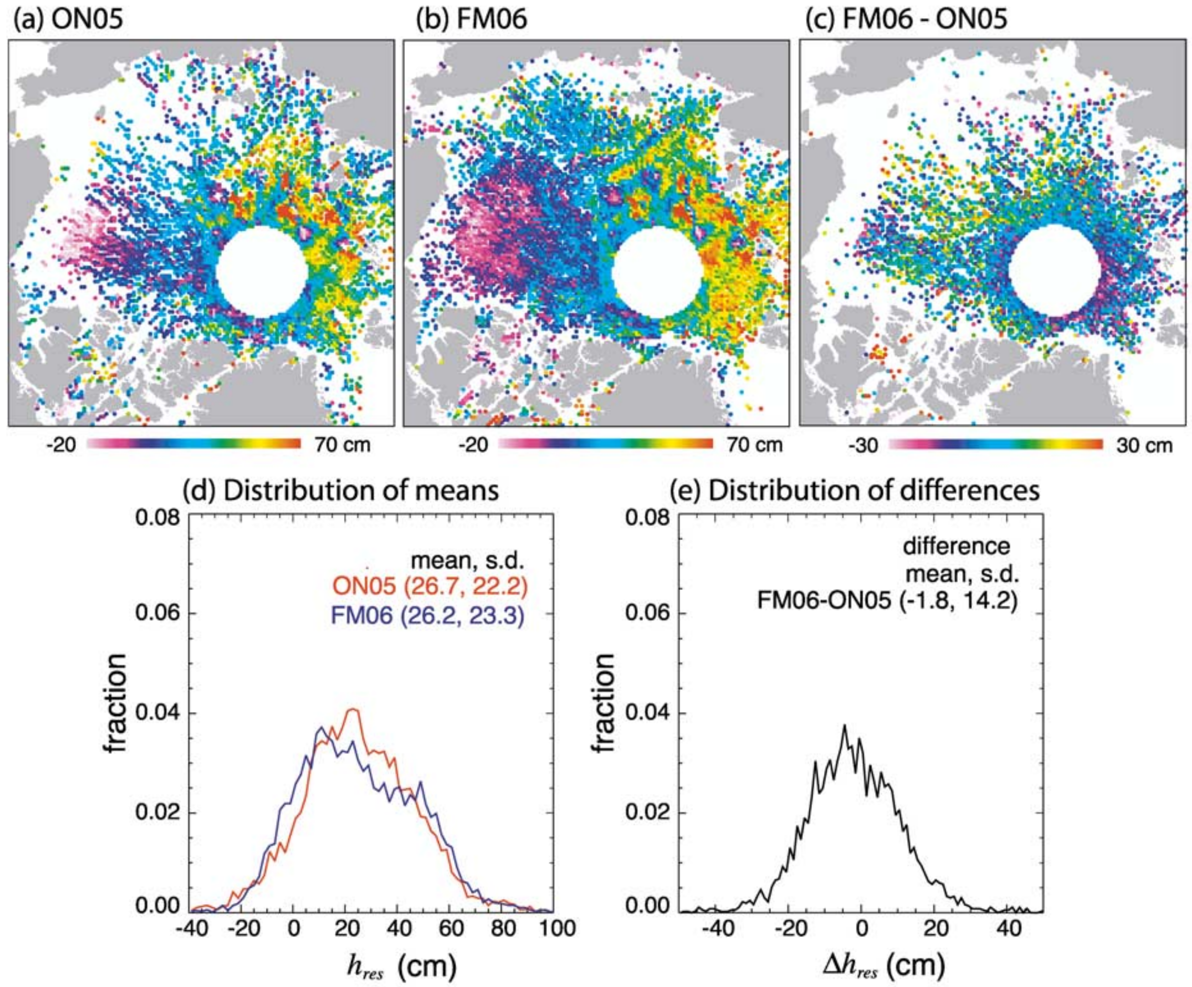

Figure 14. Residuals after subtracting the sea ice freeboard from the ICESat elevations (25-km bins; referenced to the TOPEX/POSEIDON ellipsoid). (a) ON05. (b) FM06. (c) Difference between FM06 and ON05. (d) Distribution of the ON05 and FM06 residual elevations. (e) Distribution of their differences.

spatial field is seen in their difference. It appears that these correlated patterns are associated with a component of h'_{ssh} that is due largely to shorter-wavelength residuals in the static geoid and perhaps mean dynamic topography. Large-scale expressions of the bathymetric relief can be seen: the relatively flat Canada Basin and Siberian Shelf, and the more complex relief of ocean plateaus and troughs south of the Nansen Basin stand out. Assuming the statistics of the difference field to be a measure of the energy in the time-varying/noise component, the variance of the residual static field can be estimated as: $[(23)^2 - (14/\sqrt{2})^2]$ cm^2 or $(22)^2$ cm^2. The factor of $1/\sqrt{2}$ accounts for the fact that Figure 14e corresponds to the difference between two fields, both of which includes a random component. The static component of h'_{ssh} accounts for $\sim(23 \text{ cm})^2$ of the variance compared to $\sim(10 \text{ cm})^2$ for the time-varying or random component. The larger static term is not unexpected: the spatial variability of the geoid is more energetic than the other terms in equation (3) at all length scales [*Chelton et al.*, 2001; *Wagner*, 1979].

[53] Throughout the development, we have assumed $\bar{h}_{25km}$ to be a good initial estimate of h'_{ssh} with embedded sea ice. The results here provide qualitative support that this assumption seems reasonable: the near equivalence of the distribution of the two h'_{ssh} fields; their correlated spatial patterns; and, there is little trace of the ice cover in the difference field. Thus it seems that the 25-km filtered mean is effective in separating initially the length scales of variability of the sea ice cover and that of the sea surface.

8. Summary and Conclusions

[54] In this examination of ICESat data, we focus on the identification of sea surface tiepoints for the retrieval of freeboard and the assessment of their uncertainties. The two ICESat data sets that are used allow us to assess the seasonal consistency in the retrieved freeboard fields. Three approaches that yield tiepoints of different qualities are discussed. The best quality tiepoints are from those of young ice in new openings identified in ICESat profiles and SAR imagery. An intermediate quality category of

tiepoints is obtained by comparing the reflectivity of the samples with that of the background ice and the expected deviation of these samples from a mean surface. A third category uses only the expected deviation of these samples from a mean surface as the selection criterion. The strength of the second and third approaches is that they do not depend on SAR imagery and offer a larger number of tiepoints for providing a more complete view of the spatial pattern of sea ice freeboard over the Arctic Basin. However, because of the nature of these tiepoints, they are expected to underestimate the freeboard by up to several centimeters (<4 cm) on the basis of our assessment. Using the tiepoints from new openings as a reference, the uncertainty in the individual tiepoints from these two approaches is $\sim$5 cm. We would like to emphasize, however, that one has a choice of quality over density if only sparsely distributed tiepoints of the highest quality (like those in Figure 3) are of interest.

[55] The preferred estimate of sea surface is created from the weighted average of the two categories of tiepoints within 25-km ICESat segments. Estimates from these segments are binned to construct gridded fields of mean freeboard. The within-bin variability of $\sim$3 cm indicates that not only are the 25-km estimates consistent, but that the spatial and temporal variability of the mean freeboard estimates are relatively small at this length scale. Our present assessment provides one indication of what could be achievable. The results suggest that our retrieval procedures could provide consistent freeboard estimates along 25-km segments with uncertainties of better than 7 cm (i.e., $\sqrt{(4^2 + 5^2)}$ cm); the actual uncertainties are, of course, dependent on the number of tiepoints available within each segment. Pointwise absolute estimation freeboard uncertainties, however, are more difficult to obtain. It is subject to systematic (instrument and processing) and nonsystematic errors (e.g., variability in surface returns, sea surface variability) that are often difficult to quantify. Spatial averaging would reduce these errors only if they are well behaved.

[56] Separating the freeboard distributions of the seasonal and perennial ice, we find that the mean freeboards of multiyear (MY) and first-year (FY) ice to be 35 cm and 14 cm in the fall, and 44 cm and 27 cm in the winter. The increases in mean freeboard of $\sim$9 cm and $\sim$12 cm on MY and FY sea ice are associated with ice growth and snow accumulation during the four months between data acquisitions. The freeboard distributions of the seasonal ice cover (with S.D.s of $\sim$5 cm) are sharply peaked in both the fall and winter because of ice of similar age (within weeks). The higher variability in the age and deformation of the MY ice cover contribute to the larger S.D. (of $\sim$15 cm).

[57] The ICESat freeboards are compared with the freeboard derived from the snow and ice thickness measurements reported by ice mass balance buoys. For the five data points available, the agreement seems remarkable considering the ICESat estimates are on a fairly coarse spatial scale compared to the point measurements provided by IMBs; but enthusiasm should be tempered by the fact that the errors in freeboard is multiplied tenfold in the conversion to errors in ice thickness. The placement of these buoys on relatively level MY ice helps since the measured ice thickness and snow cover could be expected to be somewhat closer to the larger-scale average. It is also interesting to note (from the IMB measurements) that changes in snow depth accounts for 90% of the increase in freeboard of MY ice between late October and late February since the contribution of ice growth to the overall freeboard is lower over thick ice. Thus seasonal changes in ICESat freeboard over old ice are good estimates of changes in snow depth. Conversely, accurate estimates of snow depth are critical for detecting seasonal changes in MY ice thickness. This also highlights the fact that a time series of ICESat freeboard provides a good indicator of seasonal changes in snow depth. Over FY ice, however, the contribution of ice growth to freeboard would be higher. Though the number of data points used in this comparison is small, it serves to illustrate that a few well-placed buoys could be useful for the validation of ICESat sea ice freeboard retrievals if it could be demonstrated, with a larger data set, that point measurements from IMBs are indeed useful after considering the issues discussed in section 6. The argument for using IMB data at this stage is that they provide direct measurements of total freeboard (ice and snow); upward looking sonars provide ice drafts and an additional level of snow depth uncertainty is introduced when draft is converted to freeboard. Of course, ULS ice draft is the data of choice once we have ice thickness derived from ICESat.

[58] Removal of the sea ice contribution and modeled sea surface heights from the two ICESat data sets gives two residual fields of unexplained sea surface height of similar variance ($\sim$23 cm) that are spatially correlated. It appears that these correlated patterns are associated with a component that is due largely to residuals in the static geoid and perhaps mean dynamic topography. These patterns seem to be associated with large-scale expressions of the bathymetric relief of the Arctic Ocean: the relatively flat Canada Basin and Siberian Shelf, and the more complex relief of ocean plateaus and troughs south of the Nansen Basin stand out. Differencing the two residual fields yield a relatively random spatial field with a negligible mean ($\sim$2 cm) and reduced variance. The absence of any patterns in the difference field that resembles the ice cover gives additional support, albeit qualitative, to our retrieved freeboard fields. We estimate that the static component accounts for $\sim$(23 cm)^2 of the variance of the residual field compared to $\sim$(10 cm)^2 for the time-varying or random component. We expect that the static field could be used to improve the geoid and the mean dynamic topography of the Arctic Ocean.

[59] The present examination of ICESat data is focused on freeboard retrieval but of more immediate geophysical interest is of course ice thickness. We have offered three retrieval procedures and assessed their results, but have not taken the next steps to convert total freeboard to ice thickness. The tenfold multiplication of the freeboard uncertainties in the conversion process is intimidating. Although these uncertainties could be reduced by spatial averaging, this places stringent demands on measurement accuracy. The next step is challenging because it requires knowledge of the spatial distribution of snow depth. The best snow depth climatology [*Warren et al.*, 1999] was developed using data from 1954 through 1991; thus it is not clear how this compilation reflects present-day snow conditions. In addition, it is representative only of snow depth over level MY ice. With the larger expanse of seasonal ice over the Arctic and the later onset of snow accumulation, it is uncertain how one could apply the climatology over these

regions. The snow depth estimates over the seasonal ice cover being developed by *Markus et al.* [2006] using multichannel passive microwave radiometry hold promise but await more extensive validation. As discussed earlier, it is also important to recognize that there is a large snow signal in the ICESat freeboard. Since the changes in freeboard over MY ice are mostly due to snow, it could serve as a constraint on snow/ice thickness retrieval if a denser temporal sampling of freeboard were available. It is unfortunate though that the current ICESat sampling of the Arctic is restricted to only three times a year due to limitations in laser lifetime. With that, our attention and effort are now turned toward answering the following question: What is achievable, in terms of accuracy, in the conversion of ICESat freeboard to sea ice thickness?

[60] **Acknowledgments.** We wish to thank D. Perovich for providing the snow depth and ice thickness data from the ice mass balance buoys deployed during the fall of 2005 and winter of 2006. The RADARSAT image data are provided by the Alaska Satellite Facility, Fairbanks, Alaska. The AMSR-E brightness temperature and ice concentration fields were provided by World Data Center A for Glaciology/National Snow and Ice Data Center, University of Colorado, Boulder, Colorado. This work was carried out at the Jet Propulsion Laboratory, California Institute of Technology, under contract with the National Aeronautics and Space Administration.

References

Brenner, A. C., et al. (2003), Derivation of range and range distributions from laser pulse waveform analysis for surface elevations, roughness, slope, and vegetation heights: Algorithm theoretical basis document version 3.0, report, NASA Goddard Space Flight Center, Greenbelt, Md.

Chelton, D. B., J. C. Ries, B. J. Haines, L. Fu, and P. S. Callahan (2001), Satellite altimetry, in *Satellite Altimetry and Earth Sciences*, *Int. Geophys. Ser.*, vol. 19, pp. 1–131, Academic Press, San Diego, Calif.

Forsberg, R., and H. Skourup (2005), Arctic Ocean gravity, geoid and sea-ice freeboard heights from ICESat and GRACE, *Geophys. Res. Lett.*, *32*, L21502, doi:10.1029/2005GL023711.

Kovacs, A. (1996), Sea ice: Part II. Estimating the full-scale tensile, flexural, and compressive strength of first-year ice, *CRREL Rep. 96-11*, Cold Reg. Res. and Eng. Lab., Hanover, N. H.

Kwok, R. (2002), Sea ice concentration estimates from satellite passive microwave radiometry and openings from SAR ice motion, *Geophys. Res. Lett.*, *29*(9), 1311, doi:10.1029/2002GL014787.

Kwok, R. (2004), Annual cycles of multiyear sea ice coverage of the Arctic Ocean: 1999–2003, *J. Geophys. Res.*, *109*, C11004, doi:10.1029/2003JC002238.

Kwok, R., A. Schweiger, D. A. Rothrock, S. Pang, and C. Kottmeier (1998), Sea ice motion from satellite passive microwave data assessed with ERS SAR and buoy data, *J. Geophys. Res.*, *103*(C4), 8191–8214.

Kwok, R., H. J. Zwally, and D. Yi (2004), ICESat observations of Arctic sea ice: A first look, *Geophys. Res. Lett.*, *31*, L16401, doi:10.1029/2004GL020309.

Kwok, R., G. F. Cunningham, H. J. Zwally, and D. Yi (2006), ICESat over Arctic sea ice: Interpretation of altimetric and reflectivity profiles, *J. Geophys. Res.*, *111*, C06006, doi:10.1029/2005JC003175.

Laxon, S., N. Peacock, and D. Smith (2003), High interannual variability of sea ice in the Arctic region, *Nature*, *425*, 947–950.

Markus, T., D. C. Powell, and J. R. Wang (2006), Sensitivity of passive microwave snow depth retrievals to weather effects and snow evolution, *IEEE Trans Geosci. Remote Sens.*, *44*(1), 68–77.

Martin, S., R. Drucker, and M. Fort (1995), A laboratory study of frost flower growth on the surface of young sea ice, *J. Geophys. Res.*, *100*(C4), 7027–7036.

Melling, H., and D. A. Riedel (1996), Development of the seasonal pack ice in the Beaufort Sea during winter of 1991–1992: A view from below, *J. Geophys. Res.*, *101*(C5), 11,975–11,991.

Schutz, B. E., H. J. Zwally, C. A. Shuman, D. Hancock, and J. P. DiMarzio (2005), Overview of the ICESat Mission, *Geophys. Res. Lett.*, *32*, L21S01, doi:10.1029/2005GL024009.

Schwarz, J., and W. F. Weeks (1977), Engineering properties of sea ice, *J. Glaciol.*, *19*(81), 499–530.

Wagner, C. (1979), The geoid spectrum from altimetry, *J. Geophys. Res.*, *84*(B8), 3861–3870.

Warren, S. G., I. G. Rigor, N. Untersteiner, V. F. Radionov, N. N. Bryazgin, Y. I. Aleksandrov, and R. Colony (1999), Snow depth on Arctic sea ice, *J. Clim.*, *12*(6), 1814–1829.

Weeks, W. F., and O. S. Lee (1958), Observation on the physical properties of sea ice at Hopedale, Labrador, *Arctic*, *11*(3), 134–155.

Wiscombe, W. J., and S. G. Warren (1980), A model for spectral albedo of snow: I, *Pure snow, J. Atmos. Sci.*, *37*(12), 2712–2733.

Zwally, H. J., et al. (2002), ICESat's laser measurements of polar ice, atmosphere, ocean, and land, *J. Geodyn.*, *24*, 405–445.

G. F. Cunningham and R. Kwok, Jet Propulsion Laboratory, California Institute of Technology, 4800 Oak Grove Drive, Pasadena, CA 91109, USA. (ron.kwok@jpl.nasa.gov)

D. Yi, SGT, Inc., NASA Goddard Space Flight Center, Greenbelt, MD 20771, USA.

H. J. Zwally, Cryospheric Sciences Branch, Code 614.1, NASA Goddard Space Flight Center, Greenbelt, MD 20771, USA.